DOI: https://doi.org/10.14256/JCE.4339.2025

Primljen / Received: 9.6.2025.
Ispravljen / Corrected: 23.10.2025.
Prihvaćen / Accepted: 30.10.2025.
Dostupno online / Available online: 10.4.2026.

Synergistic evolution of microstructure and coupled multiphysics mechanical responses in railway subgrades

Authors:

Ph.D. Student **Yanfu Duan**, MCE
Shihezi University, China
Faculty of Water Conservancy & Architectural Eng.
lttdyf@163.com

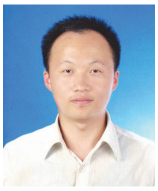

Prof. **Jianjun Cheng**, PhD. CE
Shihezi University, China
Faculty of Water Conservancy & Architectural Eng.
chengdesign@163.com
Corresponding author

Honggang Kou, MCE
Shaanxi Key Laboratory of Safety and Durability of Concrete Structures, China
13913143@qq.com

Ph.D. Student **Yaqiang Wang**, MCE
Shihezi University, China
Faculty of Water Conservancy & Architectural Eng.
Wangyq086@126.com

Original research paper

Yanfu Duan, Jianjun Cheng, Honggang Kou, Yaqiang Wang

Synergistic evolution of microstructure and coupled multiphysics mechanical responses in railway subgrades

Railway subgrades in desiccated salt lake regions are prone to swelling hazards under complex environmental conditions. To investigate the water–salt–thermal–mechanical multi-field coupling responses and the synergistic evolution of microstructure, this study examined saline soils from the Lop Nur salt lake area. A multi-physical field coupling experimental system was established to analyse mechanical responses under different environmental coupling conditions, factor sensitivity affecting mechanical parameters, microstructural evolution, and the regulatory role of pore structure in mechanical stability. Results indicate that in high-temperature zones (≥ 20 °C), shear strength is negatively correlated with water content, whereas in low-temperature zones (≤ 0 °C) a positive correlation exists. Lower temperatures also markedly suppress cumulative plastic strain. Low-temperature-induced microstructural evolution of saline soil systems proceeds through four stages: initial nucleation, chain-like growth, dynamic reconstruction, and critical failure. The synergistic evolution of multi-field coupling responses and microstructure is primarily reflected in pore structure development. These findings provide a scientific basis for evaluating mechanical stability and guiding the design and maintenance of railway subgrades in cold, arid salt lake environments.

Key words:

hydro-salt-thermal-mechanical coupling, microstructural co-evolution, railway subgrade, dry salt lake areas

Izvorni znanstveni rad

Yanfu Duan, Jianjun Cheng, Honggang Kou, Yaqiang Wang

Sinergijski razvoj mikrostrukture i vezanih multifizikalnih mehaničkih odziva donjeg ustroja željezničke pruge

Donji ustroj željezničke pruge u područjima isušenih slanih jezera sklon je deformacijama uslijed bubrenja tla u složenim okolišnim uvjetima. Radi istraživanja vezanih višepoljnih odziva u sustavu voda-sol-toplina-mehanika i sinergijskog razvoja mikrostrukture, u ovome su radu provedena ispitivanja slanih tala s područja slanog jezera Lop Nur. Uspostavljen je eksperimentalni sustav međudjelovanja multifizikalnih polja radi analize mehaničkih odziva u različitim okolišnim uvjetima povezivanja, osjetljivosti čimbenika koji utječu na mehaničke parametre, razvoja mikrostrukture te regulatorne uloge porne strukture u mehaničkoj stabilnosti. Rezultati pokazuju da je u zonama visokih temperatura (≥ 20 °C) posmična čvrstoća u negativnoj korelaciji s udjelom vode, dok u zonama niskih temperatura (≤ 0 °C) postoji pozitivna korelacija. Niže temperature također znatno smanjuju kumulativnu plastičnu deformaciju. Razvoj mikrostrukture sustava slanih tala uzrokovan niskim temperaturama ima četiri faze: početnu nukleaciju, lančani rast, dinamičku rekonstrukciju i kritični lom. Sinergijski razvoj međudjelovanja multifizikalnih odziva i mikrostrukture ponajprije se očituje u razvoju strukture pora. Ti rezultati pružaju znanstvenu osnovu za ocjenu mehaničke stabilnosti te za projektiranje i održavanje donjeg ustroja željezničke pruge u hladnim, neplodnim područjima slanih jezera.

Ključne riječi:
hidro-solno-toplinsko-mehaničko međudjelovanje, sinergijski razvoj mikrostrukture, donji ustroj željezničke pruge, područja isušenih slanih jezera

1. Introduction

The Lop Nur region, a typical desiccated salt lake in north-western China, poses significant challenges to the long-term stability of railway subgrades due to its extreme environmental conditions. Historically, Lop Nur was China's second-largest inland lake, covering an area exceeding 3,000 km^2. However, under the combined influence of climate change and human activities, it completely desiccated by the 1970s, forming a salt crust several metres thick [1-3]. As shown in Figure 1, the geographical location of the sampling point is presented; a single sampling point was used.

The current surface saline soil in Lop Nur contains salt contents as high as 30 to 50 %, with the porosity of the original saline soil ranging from 15 % to 35 %. The region experiences an extremely arid climate, with an average annual precipitation of only 20 mm, an evaporation rate exceeding 3,000 mm, and diurnal temperature variations reaching 40 °C. The crystallisation of sodium sulfate, sodium chloride, and other salts induces significant salt heave and subsidence deformation in subgrades [4, 5]. Taking the existing railway traversing Lop Nur as an example, the attenuation rate of the dynamic shear modulus of the railway subgrade remains high under long-term dynamic train loads and temperature cycling, while track surface irregularities progressively increase each year [6]. This degradation mechanism is attributed to the unique failure processes of railway subgrades in desiccated salt lake regions: the periodic dissolution–crystallisation behaviour of salt crystals reconstructs microscopic pore structures, while brine film migration between crystal interstices further weakens the soil skeleton, ultimately leading to deterioration of macroscopic mechanical properties [7-9].

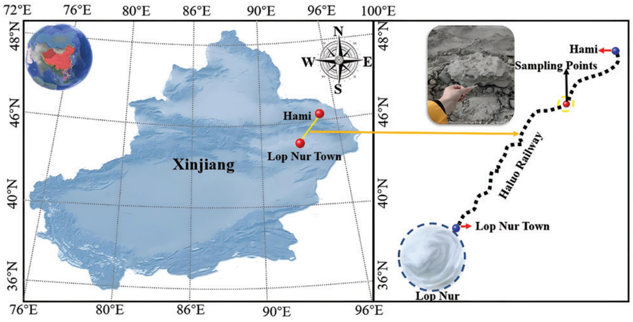

Figure 1. Geographic location of sampling sites

Current research on the mechanical behaviour of saline soils primarily focuses on responses under single physical field effects. For instance, the negative correlation between shear strength and salt content in saline soils under static loads has been validated through direct shear tests [10], while the accumulation patterns of plastic strain under dynamic loads have been preliminarily identified through dynamic triaxial tests [11, 12]. However, the complex environmental conditions in the Lop Nur region necessitate integrated investigations of multi-field coupling effects. Temperature gradients induce phase transition behaviour in saline soils, significantly altering pore structures; for example, sodium sulfate undergoes crystalline phase changes at 32.4 °C [13], while brine seepage combined with dynamic loads may accelerate crack propagation [14]. Existing studies indicate that cohesive strength decreases by 25 to 30 % when ambient temperatures exceed 30 °C; however, the underlying microscale mechanisms remain unclear [15]. Furthermore, interactions between brine salinity in salt crusts and dynamic load frequencies influence subgrade stability by modifying soil damping characteristics [16, 17]. Critical parameter sensitivities related to water, salt, temperature, and mechanical factors remain poorly defined. Most previous studies focus on isolated environmental factors (e.g., salt or temperature alone), lacking a systematic understanding of cross-scale evolution mechanisms in subgrade materials under water–salt–thermal–mechanical multi-field coupling, which significantly constrains railway engineering design and maintenance in salt lake regions [18–20]. Additionally, the coupling mechanisms between microstructural evolution and macroscopic mechanical responses in Lop Nur saline soils remain unclear. Therefore, there is an urgent need to develop a multi-physical field coupling experimental framework to elucidate the synergistic evolution of mechanical responses and microstructure in saline soils, together with a quantified attenuation model for the dynamic shear modulus.

This study establishes a multi-scale coupling analytical framework and a multi-physical field coupling experimental system for Lop Nur railway subgrades. First, orthogonal experiments with three-factor four-level and four-factor four-level designs were conducted, systematically varying water content (4 %, 6 %, 8 %, 10 %), salt content (0 %, 5 %, 10 %, 15 %), temperature (–20 °C, 0 °C, 20 °C, 40 °C), and dynamic stress amplitudes (50 kPa, 100 kPa, 150 kPa, 300 kPa) to investigate mechanical responses under multi-field coupling effects and parameter sensitivities. Second, scanning electron microscopy (SEM) was employed to correlate salt crystal morphologies with macroscopic strength parameters, thereby revealing microstructural evolution mechanisms. Concurrently, X-ray computed tomography (CT) was used to quantify pore structures in saline soils under varying water and salt contents, with coordination numbers used to evaluate the influence of pore structure on mechanical stability. Finally, a quantified attenuation model for the dynamic shear modulus was developed using orthogonal experimental data, providing a theoretical basis for predicting and controlling the mechanical behaviour of saline soils.

2. Materials and methods

2.1. Physical characterization and parameter control of saline soil materials

As shown in Figure 2.a (SEM images) and Figure 2.b (XRD pattern), scanning electron microscopy (SEM) and X-ray diffraction (XRD) analyses were conducted on field-collected soil samples. The SEM images revealed that the soil at Ha–Luo Railway K286+600 exhibits alkaline characteristics, with dominant cations including Na^+, K^+, and Ca^{2+}, and primary anions including SO_4^{2-} and Cl^-. Among the cations, Na^+ is the most abundant, followed by Ca^{2+}, while SO_4^{2-} is the predominant anion and Cl^- is present at the lowest concentration. XRD results identified the main mineral components as gypsum ($CaSO_4$), potassium sulfate (K_2SO_4), sodium sulfate (Na_2SO_4), and sodium chloride (NaCl). Chemical analysis confirmed a total salt content of 6.67 %, classifying the soil as hypersaline.

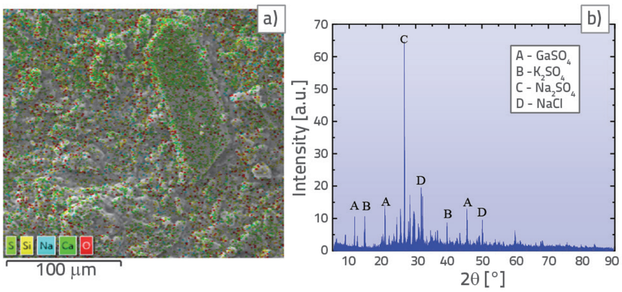

Figure 2. SEM cross-sectional imaging and X-ray diffraction (XRD) analysis: a) SEM cross-sectional image; b) XRD pattern

As shown in Figure 3, the particle size distribution and cumulative grading curves of the saline soil samples are presented. Particle size analysis revealed that samples with particle sizes > 0.075 mm exhibited poor gradation, as shown in Figure 3.c. For particles < 0.075 mm, the highest proportion was observed in the 60 to 70 µm range, as shown in Figure 3.d. The basic physical properties of the soil samples are summarised in Table 1.

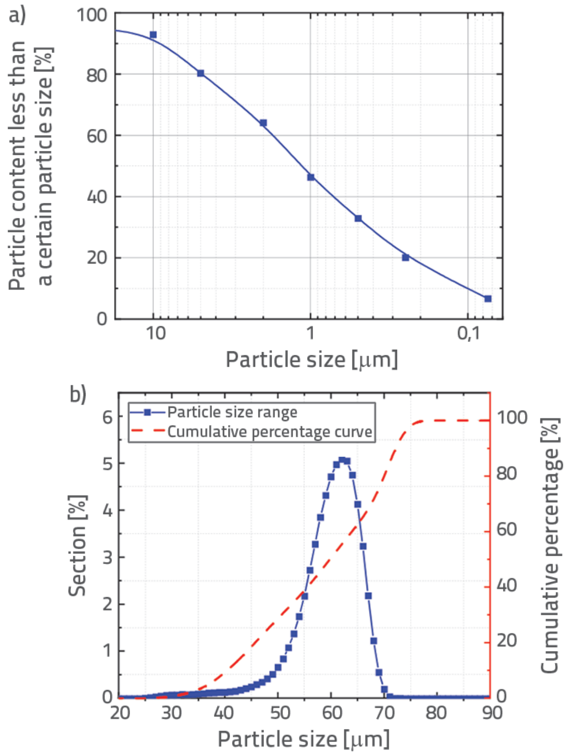

Figure 3. Particle size distribution curves: a) distribution curve of soil particles larger than 0.075 mm; b) distribution curve of soil particles smaller than 0.075 mm

2.2. Design and methodology of water–salt–thermal–mechanical coupled tests

To establish a multi-scale coupling analytical framework and a multi-physical field coupling experimental system, this study

Table 1. Physical properties of saline soil

Natural moisture content, *w* [%]	Maximum dry density [g/cm³]	Specific gravity of soil particle [G_s]	Soluble salt content [g/kg]	Atterberg limits [%]		
				Liquid limit, w_L	Plastic limit, w_P	Plasticity index, I_p
1~12.5	1.83	2.73	335.9	28.7	18	10.7

Table 2. Three-factor and four-factor orthogonal arrays with four levels

Levels	Factor				Levels	Factor			
	Water content w [%]	Salt content s [%]	Temperature t [°C]	Dynamic stress amplitude, d [kPa]		Water content w [%]	Salt content s [%]	Temperature t [°C]	Dynamic stress amplitude, d [kPa]
1	4(w_1)	0(s_1)	40(t_1)	50(d_1)	9	8(w_3)	0(s_1)	40(t_1)	50(d_1)
2	4(w_1)	5(s_2)	20(t_2)	100(d_2)	10	8(w_3)	5(s_2)	20(t_2)	100(d_2)
3	4(w_1)	10(s_3)	0(t_3)	150(d_3)	11	8(w_3)	10(s_3)	0(t_3)	150(d_3)
4	4(w_1)	15(s_4)	-20(t_4)	200(d_4)	12	8(w_3)	15(s_4)	-20(t_4)	200(d_4)
5	6(w_2)	0(s_1)	40(t_1)	50(d_1)	13	10(w_4)	0 (s_1)	40(t_1)	50(d_1)
6	6(w_2)	5(s_2)	20(t_2)	100(d_2)	14	10(w_4)	5 (s_2)	20(t_2)	100(d_2)
7	6(w_2)	10(s_3)	0(t_3)	150(d_3)	15	10(w_4)	10(s_3)	0(t_3)	150(d_3)
8	6(w_2)	15(s_4)	-20(t_4)	200(d_4)	16	10(w_4)	15(s_4)	-20(t_4)	200(d_4)

designed three-factor and four-factor, four-level orthogonal experiments with water content (4 %, 6 %, 8 %, 10 %), salt content (0 %, 5 %, 10 %, 15 %), temperature (–20 °C, 0 °C, 20 °C, 40 °C), and dynamic stress amplitude (50 kPa, 100 kPa, 150 kPa, 200 kPa). Static environmental factors included water content, salt content, and temperature, while dynamic tests incorporated an additional dynamic stress amplitude parameter. As detailed in the orthogonal arrays shown in Table 2, the static tests followed an L_{16} (4^3) design, whereas the dynamic tests used an L_{16} (4^4) configuration.

2.3. Experimental process

As shown in Figure 4, microstructural and physicochemical analyses were conducted. Soil samples were first sieved using a 2 mm sieve, followed by detailed microstructural and physicochemical characterisation. X-ray diffraction (XRD) was used to analyse mineral composition, scanning electron microscopy (SEM) for microstructural observation, energy dispersive X-ray spectroscopy (EDS) for elemental analysis, and a three-dimensional laser particle size analyser to determine particle size distribution. Remoulded saline soil specimens (w_1–s_1, w_2–s_2, w_3–s_3, w_4–s_4) were prepared by washing to remove salts, followed by drying, crushing, and sieving through a 2 mm mesh. Sodium sulfate (Na_2SO_4), the most abundant salt in the original samples, was selected as the salting agent. CT scanning was performed on the specimens with a resolution of 30 μm, operated at 220 kV and 1.3 mA at an ambient temperature of 20 °C.

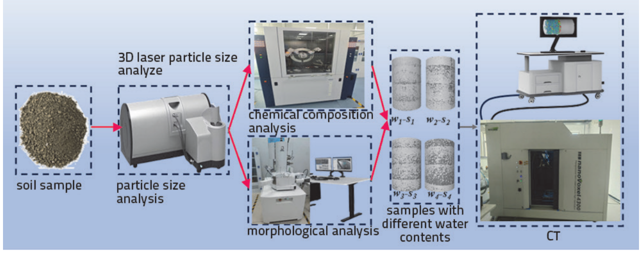

Figure 4. Microstructural and physicochemical analysis

As shown in Figure 5, the mechanical testing workflow began with specimen preparation according to the orthogonal array parameters specified in Table 2, following completion of the microstructural and physicochemical analyses. To prevent swelling failure caused by prolonged storage, tests were conducted immediately after specimen preparation. The GDS dynamic triaxial testing system (DYNTTS) was employed for both static and dynamic tests. Dynamic loading was applied using half-sine waveforms. Based on previous studies on railway subgrade loading levels, actual train loads, and vibration frequency measurements [21], the confining pressure was set to 65 kPa, the vibration frequency to 1 Hz, and the static deviatoric stress to σ_q = 15 kPa [22]. Field measurements indicate that dynamic stresses on railway subgrades range from 20 to 100 kPa. To account for potential overload conditions, dynamic stress amplitudes of 50 kPa, 100 kPa, 150 kPa, and 200 kPa were applied. The test was terminated when the axial cumulative strain reached 5 % or the number of loading cycles reached 10,000.

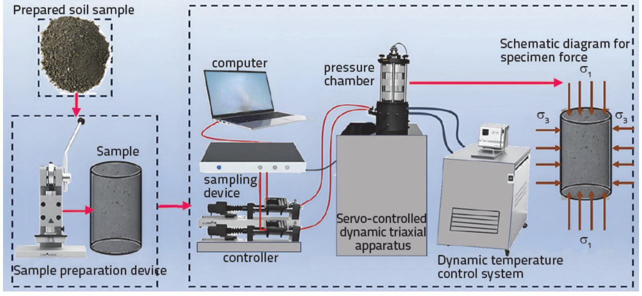

Figure 5. Mechanical testing procedure

3. Hydro–thermal–salt–mechanical multi-field coupling mechanical response of railway subgrades in arid salt lake regions

3.1. Static-dynamic response analysis

As shown in Figures 6.a to 6.d, axial stress–axial strain curves were obtained, and the peak shear strengths derived from these curves were statistically analysed to produce Figure 6.e. Figure 6.e illustrates the coupled effects of salt content, temperature, and water content on shear strength under a confining pressure of 65 kPa. The results indicate that in high-temperature zones (≥ 20 °C), shear strength is negatively correlated with water content, whereas in low-temperature zones (≤ 0 °C), shear strength is positively correlated with water content. For instance, at 0 % salt content and 40 °C, specimens with water contents of 4 %, 6 %, 8 %, and 10 % exhibited shear strengths of 350 kPa, 296 kPa, 236 kPa, and 182 kPa, respectively, representing a 48 % reduction as water content increased from 4 % to 10 %. Conversely, at 15 % salt content and –20 °C, specimens with water contents of 4 %, 6 %, 8 %, and 10 % showed shear strengths of 722 kPa, 1019 kPa, 1047 kPa, and 1269 kPa, respectively, indicating a 43 % increase with increasing water content. This phenomenon suggests that higher water content amplifies the strengthening effect at low temperatures, likely due to ice crystal formation below 0 °C, which enhances interparticle cohesion through cementation and reinforces salt crystallisation, forming a rigid framework that improves overall material strength. These findings highlight the significant coupling effects of water content and temperature on shear strength.

When water content remains constant, shear strength increases substantially under combined conditions of higher salt content and lower temperature. For example, at 10 % water content, shear strengths for s_1-t_1, s_2-t_2, s_3-

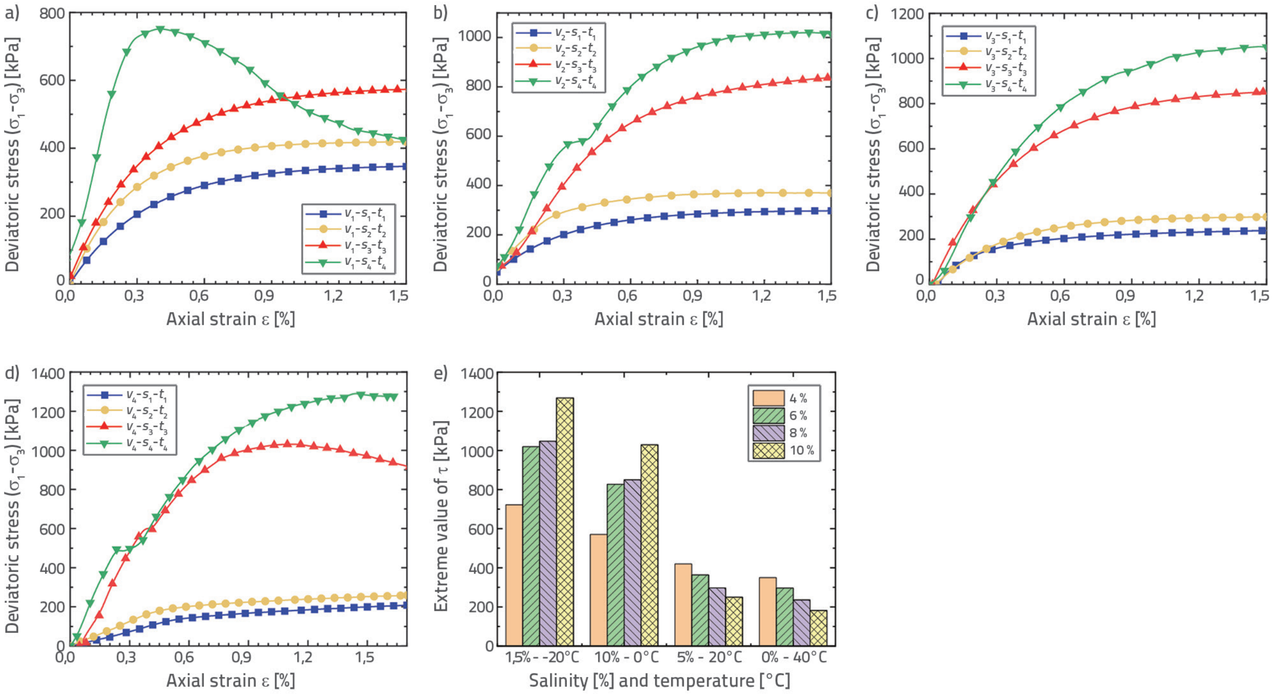

Figure 6. Axial stress–axial strain relationship and peak shear strength: a) sample with 4 % water content; b) sample with 6 % water content; c) sample with 8 % water content; d) sample with 10 % water content; e) peak shear strength

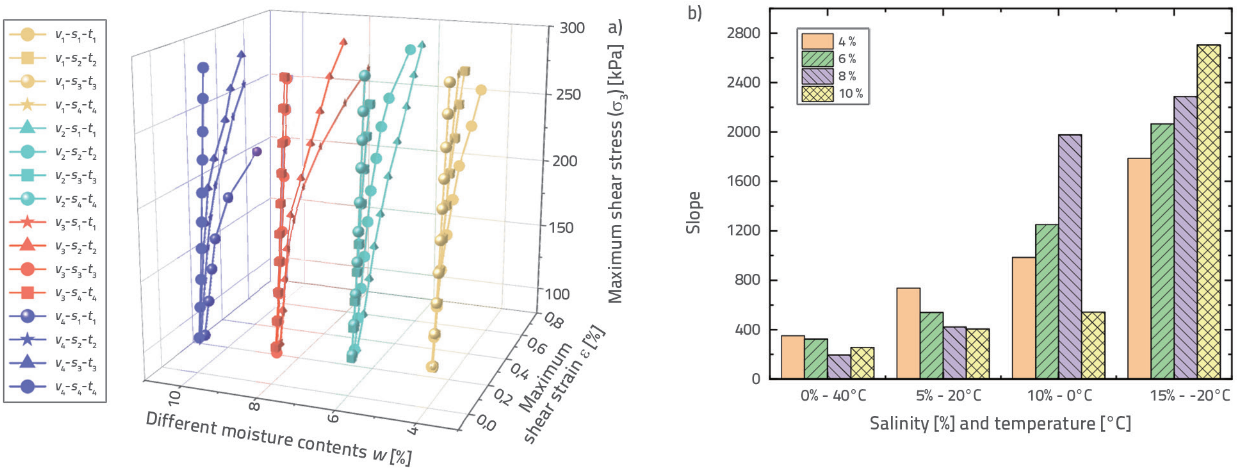

Figure 7. Backbone curve and peak slope: a) backbone curve; b) peak slope of the backbone curve

t_3, and s_4-t_4 reached 182 kPa, 250 kPa, 1029 kPa, and 1269 kPa, respectively. Similarly, at 4 % water content, the corresponding shear strengths were 350 kPa, 420 kPa, 571 kPa, and 722 kPa, respectively. This behaviour occurs because salt solubility increases with temperature, leading to partial dissolution of salt crystals into ions, which weakens interparticle bonding and reduces strength. Conversely, at low temperatures, salts and ice crystals co-form composite cementitious structures, enhancing structural stability [23]. These results further indicate that elevated temperatures accelerate salt dissolution and water migration, thereby weakening interparticle bonding.

3.2. Dynamic response analysis

3.2.1. Analysis of force-backbone curve slope under dynamic loading

As shown in Figure 7.a (backbone curves) and Figure 7.b (slope extrema), the backbone curve slopes were derived from the peak shear strengths presented in Figure 7.a. Figure 7.b shows that the backbone curve slopes increased significantly with decreasing temperature across all test conditions, indicating a positive correlation between temperature reduction and slope magnitude. Both salt content and temperature exhibited

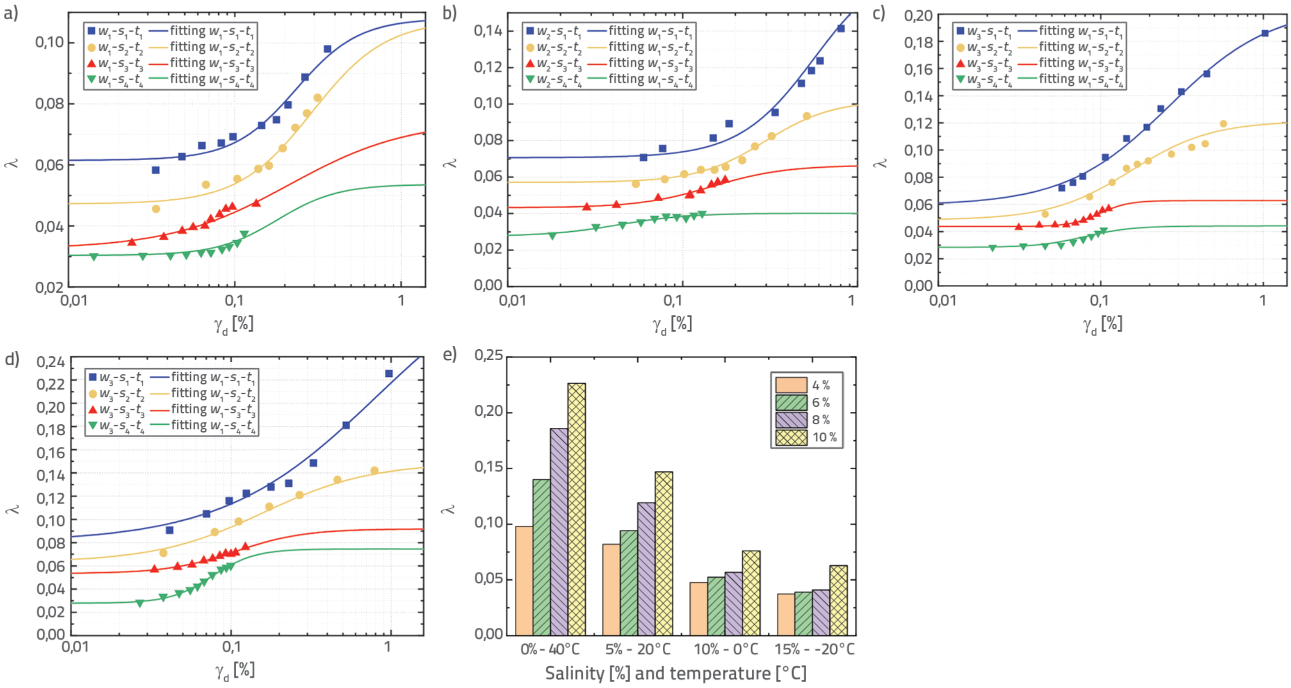

Figure 8. Shear strain–damping ratio relationship and peak damping ratio: a) sample with 4 % water content; b) sample with 6 % water content; c) sample with 8 % water content; d) sample with 10 % water content; e) peak damping ratio

positive correlations with the backbone curve slopes, while water content showed both positive and negative relationships. For example, at 4 % water content, the backbone curve slopes for specimens w_1-s_1, w_1-s_2, w_1-s_3 and w_1-s_4 (corresponding to 40 °C, 20 °C, 0 °C, and –20 °C) were 351, 736, 985, and 1786, respectively, demonstrating a 408.83 % increase from 40 °C to –20 °C. At 10 % water content, the slopes for w_4-s_1, w_4-s_2, w_3-s_3, and w_4-s_4 (under identical temperature gradients) were 256, 405, 543, and 2705, showing a 956.64 % increase. This suggests that ice crystal network formation at low temperatures enhances internal stress transfer efficiency, leading to significant increases in slope and confirming the dominant role of temperature in slope development.

In high-temperature zones (≥20 °C), backbone curve slopes were negatively correlated with water content, whereas in low-temperature zones (≤0 °C), positive correlations were observed. For instance, at 0 % salt content and 40 °C, slopes for specimens with 4 %, 6 %, 8 %, and 10 % water content were 352, 324, 295, and 255, respectively, representing a 27.45 % decrease with increasing water content. Conversely, at 15 % salt content and –20 °C, slopes for specimens with 4 %, 6 %, 8 %, and 10 % water content reached 1786, 2066, 2288, and 2705, representing a 295.3 % increase with increasing water content. This behaviour occurs because moisture acts as a lubricant at high temperatures, weakening intermolecular forces, whereas at low temperatures, phase transitions form rigid ice crystal frameworks. These synergistic effects between water content and temperature highlight the nonlinear modulation of temperature responses by moisture conditions.

3.2.2. Damping ratio analysis under dynamic loading

As shown in Figures 8.a to 8.d, the relationship between shear strain and damping ratio is presented. In the curves, γ denotes the damping ratio and, γ_d represents the shear strain, while Figure 8.e shows the maximum damping ratio under the 16 test conditions. Figure 8.e indicates that decreasing temperature systematically reduces γ, with the magnitude of cooling positively correlated with damping ratio attenuation. Taking the specimen with 4 % water content as an example, at temperatures of 40 °C, 20 °C, 0 °C, and –20 °C, the damping ratios for specimens w_1-s_1, w_1-s_2, w_1-s_3, and w_1-s_4 were 0.098, 0.082, 0.07611, and 0.0629, respectively, corresponding to a 35.81 % reduction from 40 °C to to 20 °C. For the 10 % water content specimens, $w4$–s_1, w_4-s_2, w_4-s_3 and w_4-s_4 exhibited damping ratios of 0.2265, 0.147, 0.0477, and 0.03754 across the same temperature gradient, demonstrating an 83.42 % decrease. These findings indicate that low temperatures suppress the mobility of molecular chain segments within the material, reducing energy dissipation pathways and consequently diminishing damping capacity, thereby confirming the dominant controlling effect of temperature on damping characteristics.

Figure 8.e further demonstrates that increased water content amplifies temperature-dependent variations in the damping ratio. At 0 % salt content, specimens w_1-t_1, w_2-t_1, w_3-t_1, and w_4-t_1 showed damping ratios of 0.098, 0.14, 0.1859, and 0.2265, respectively. Conversely, at 15 % salt content, specimens w_1-t_4, w_2-t_4, w_3-t_4, and w_4-t_4 exhibited damping ratios of 0.0629, 0.0411, 0.0411, and 0.03754, respectively. This indicates

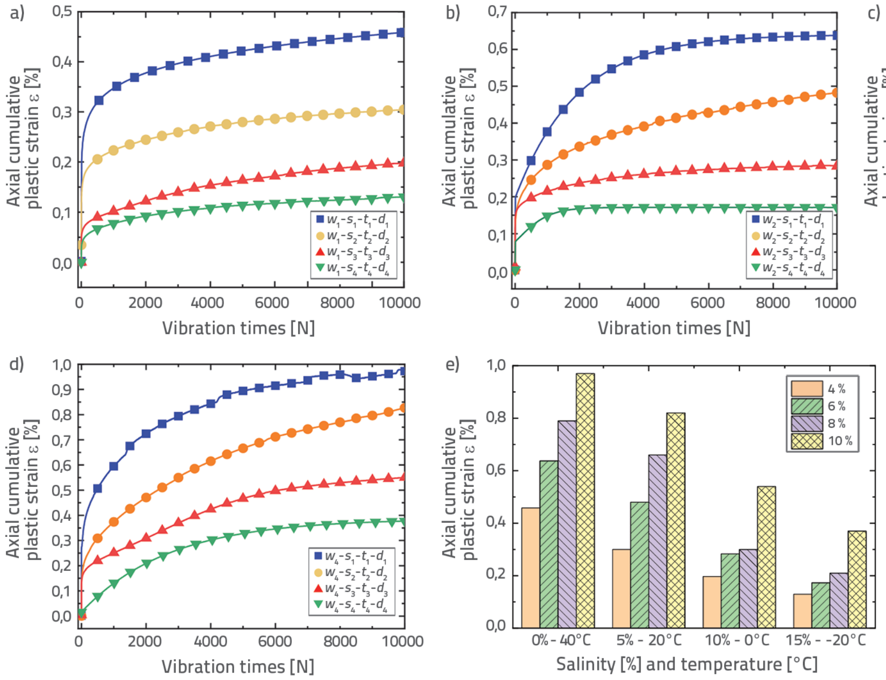

Figure 9. Relationship between vibration cycles and cumulative plastic strain ε and extremum values of cumulative plastic strain: a) sample with 4 % water content; b) sample with 6 % water content; c) sample with 8 % water content; d) sample with 10 % water content; e) extremum values of cumulative plastic strain ε

a positive correlation between water content and damping ratio in high-temperature regimes, contrasted with a negative correlation in low-temperature regimes. The underlying mechanisms involve:

- the formation of dense ice crystal networks in high-moisture materials at low temperatures, which restrict local molecular chain mobility and significantly reduce energy dissipation capacity;
- increased ion concentrations in pore fluids due to salt dissolution at elevated temperatures, which reduce viscous resistance.

3.2.3. Analysis of cumulative plastic strain under dynamic loading

As shown in Figures 9.a to 9.d, the curves depict the relationship between vibration cycles and cumulative plastic strain (ε), while Figure 9.e summarises the extreme ε values across 16 experimental conditions. Figure 9.e shows that decreasing temperature significantly suppresses cumulative plastic strain (ε), with lower temperatures corresponding to smaller ε values. For instance, specimens $w_1–s_1$, $w_1–s_2$, $w_1–s_3$, and $w_1–s_4$ exhibited ε values of 0.458, 0.63, 0.79, and 0.97 at 40 °C, respectively, which decreased to 0.13, 0.173, 0.21, and 0.37 at –20 °C, corresponding to reductions of 71.62 % and 61.86 %, respectively. This indicates that low temperatures enhance interfacial bonding within the material lattice, restrict dislocation movement and creep rates, and thereby substantially reduce plastic strain. These results confirm the decisive role of temperature in governing cumulative plastic strain (ε).

When the salt content is 0 %, increasing water content from 4 % to 10 % increases ε from 0.458 to 0.97 at 40 °C. Conversely, under 15 % salt content and –20 °C, ε values for the same water content range decrease to 0.13–0.37. This establishes a positive correlation between ε and both water content and salt content. The underlying mechanism involves ion shielding effects: Na^+ and SO_4^{2-} ions adsorb onto grain boundaries, reducing the effective contact area between soil particles and increasing their susceptibility to slippage. This phenomenon suggests that water content exerts differential interference on temperature sensitivity.

3.2.4. Analysis of dynamic shear modulus under dynamic loading

As shown in Figures 10.a to 10.d, the curves illustrate the relationship between shear strain and dynamic shear modulus (G_d), while Figure 10.e summarises the extreme G_d values across 16 experimental conditions. The results indicate that decreasing temperature significantly increases G_d, with higher water content corresponding to lower G_d and higher salt content corresponding to higher G_d. For example, specimens $w_1–s_1$, $w_1–s_2$, $w_1–s_3$, and $w_1–s_4$ exhibited G_d values of 29 MPa, 102 MPa, 130 MPa, and 194 MPa at 40 °C, respectively, increasing to 194 MPa at –20 °C, representing a 668.96 % increase. Similarly, specimens $w_4–s_1$, $w_4–s_2$, $w_4–s_3$, and $w_4–s_4$ showed G_d values increasing from 21 MPa to 831 MPa as temperature

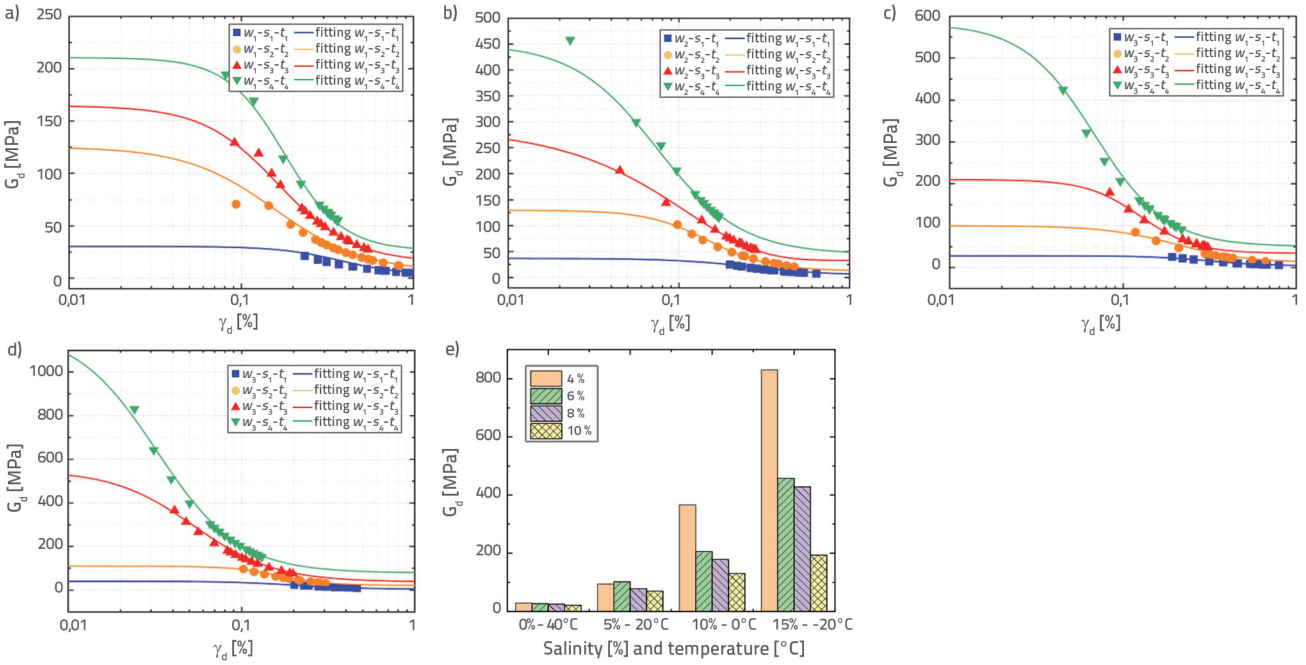

Figure 10. Shear strain–dynamic shear modulus relationship and peak dynamic shear modulus values: a) sample with 4 % water content; b) sample with 6 % water content; c) sample with 8 % water content; d) sample with 10 % water content; e) peak dynamic shear modulus values

Table 3. Orthogonal test results

Factors	Outcomes					Factors	Outcomes				
	Shear strength τ [kPa]	Damping ratio γ	Slope I	Cumulative plastic strain ε [%]	Dynamic shear modulus G_d [MPa]		Shear strength τ [kPa]	Damping ratio γ	Slope I	Cumulative plastic strain ε [%]	Dynamic shear modulus G_d [MPa]
1	350	0.098	351.564	0.458	29	9	236	0.1859	195.2401	0.79	130
2	420	0.082	736.1974	0.3	27	10	297	0.11936	421.8759	0.66	179
3	571	0.07611	985.4184	0.197	25	11	850	0.0569	1977.134	0.3	206
4	722	0.0629	1786.865	0.13	21	12	1047	0.0411	2288.167	0.21	366
5	296	0.14	324.3725	0.637	102	13	182	0.2265	255.9431	0.97	194
6	364	0.09431	539.2929	0.48	94	14	250	0.147	404.9258	0.82	428
7	827	0.0569	1249.603	0.283	78	15	1029	0.0477	542.7306	0.54	458
8	1019	0.0411	2066.909	0.173	70	16	1269	0.03754	2705.265	0.37	831

decreased from 40 °C to −20 °C, representing a 3957.14 % increase. This behaviour occurs because high temperatures reduce intergranular cohesion through salt dissolution and water lubrication, whereas low temperatures promote the formation of ice–salt crystal networks that reinforce structural rigidity. These findings confirm the nonlinear regulatory role of temperature in the dynamic shear modulus (G_d).

At 0 % salt content and 40 °C, G_d values for specimens with water contents of 4 %, 6 %, 8 %, and 10 % were 29 MPa, 27 MPa, 25 MPa, and 21 MPa, respectively, representing a 27.58 % decrease with increasing water content. Conversely, under 15 % salt content and −20 °C, G_d values for the same water content range increased to 194 MPa, 428 MPa, 458 MPa, and 831 MPa, demonstrating a 428.35 % increase. This reveals an inverse correlation between G_d and water content in high-temperature regimes (≥ 20 °C), contrasted with a positive correlation in low-temperature regimes (≤ 0 °C). The underlying mechanisms involve:

- high-temperature water lubrication of grain boundaries, reducing shear resistance;
- the formation of salt–ice crystal networks in low-temperature, high-moisture samples, which amplify thermal strengthening effects through volumetric constraints.

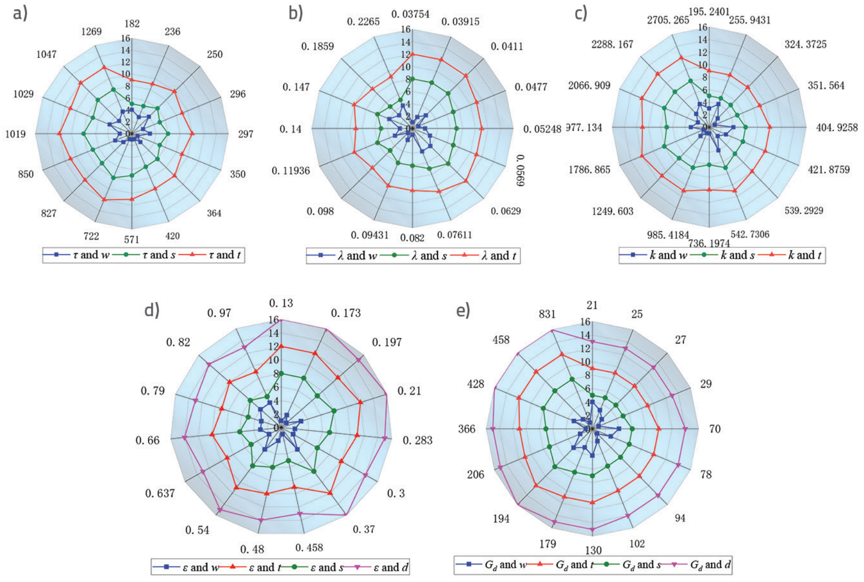

Figure 11. Comparative radar charts: a) shear strength variance analysis; b) damping ratio variance analysis; c) backbone curve slope variance analysis; d) cumulative plastic strain variance analysis; e) dynamic shear modulus variance analysis

3.3. Sensitivity analysis of static and dynamic parameters

The orthogonal experimental results are summarised in Table 3. Based on the extreme values of shear strength (Figure 6.e), damping ratio (Figure 7.e), backbone curve slope (Figure 8.e), cumulative plastic strain (Figure 9.e), and dynamic shear modulus (Figure 10.e), the extreme values of the mechanical test data were compiled in Table 1. Variance analysis was subsequently conducted to quantify the sensitivity of each factor influencing the mechanical parameters. This systematic approach enabled the identification of the key parameters controlling material behaviour under combined water–salt–thermal–mechanical conditions, providing important insights for geotechnical engineering applications in cold regions.

Figures 11.a to 11. c present variance radar charts for shear strength, damping ratio, and backbone curve slope, respectively. The results indicate that water content exhibits the highest variability in the two-dimensional radar charts, while salt content and temperature display similar magnitudes of fluctuation, both lower than that of water content. The sensitivity hierarchy for these three factors is identified as: water content > salt content = temperature. Figures 11.d and 11.e show variance radar charts for cumulative plastic strain and dynamic shear modulus. The analysis reveals a maximum variance value of 45.4 for water content, whereas salt content, temperature, and dynamic stress amplitude form a sensitivity cluster with variance values ranging from 6.1 to 8.9. The sensitivity ranking is water content > salt content = temperature = dynamic stress amplitude, demonstrating that water content exerts the most significant influence on mechanical responses under coupled water–salt–thermal–mechanical conditions. This finding underscores the dominant role of water content in controlling the behaviour of geotechnical materials in cold regions.

3.4. Co-evolutionary analysis of microstructure

3.4.1. Regulatory mechanisms of pore structure evolution on mechanical stability

Figures 12.a to 12.d show SEM images under w_1–s_1–t_1, w_2–s_2–t_2, w_3–s_3–t_3, and w_4–s_4–t_4 environmental conditions, respectively. From Figures 12.a and 12.b, numerous pores are observed within

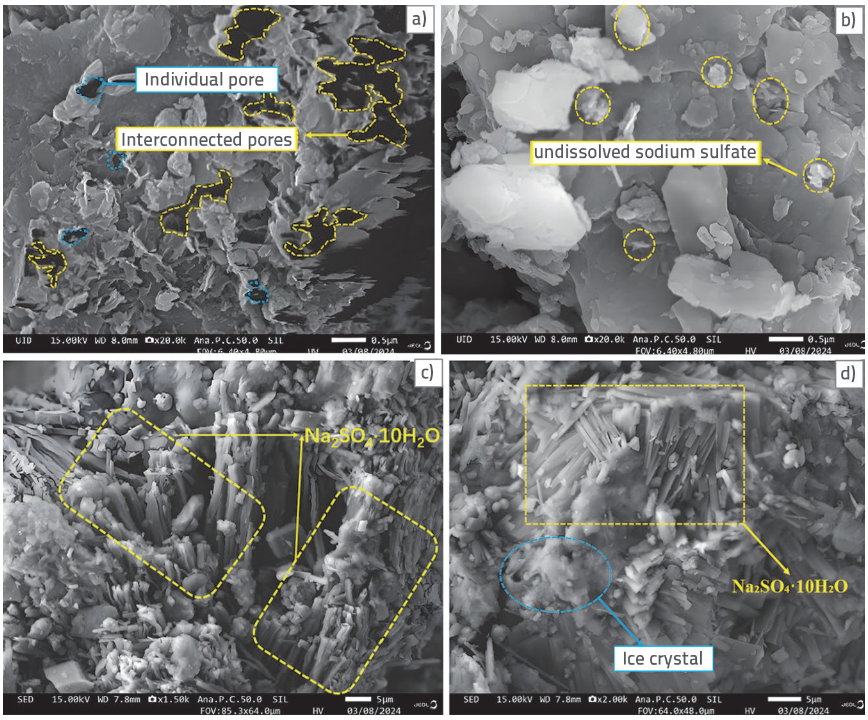

Figure 12. SEM images under different environmental conditions: a) w_1–s_1–t_1**; b)** w_2–s_2–t_2**; c)** w_3–s_3–t_3**; d)** w_4–s_4–t_4

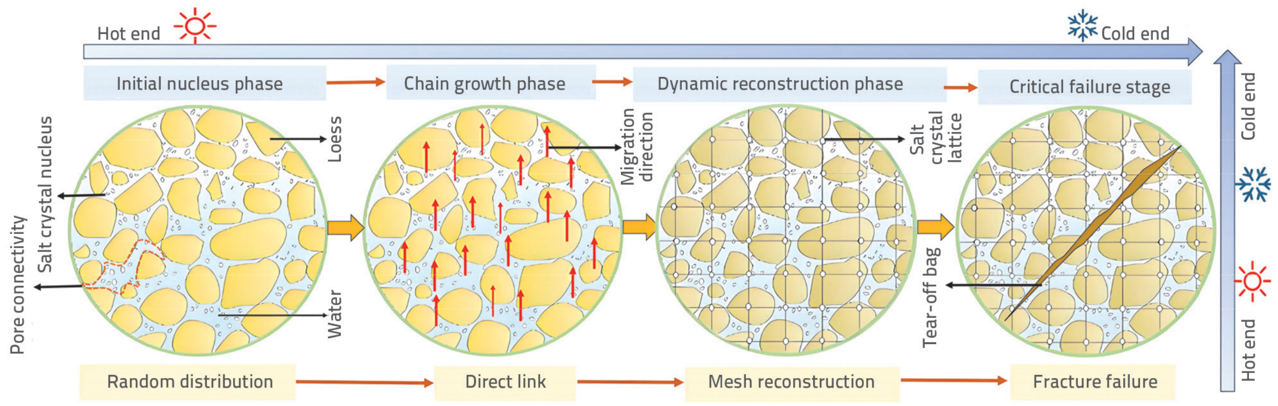

Figure 13. Schematic diagram of the microstructure co-evolution process

the soil particles, whereas Figures 12.c and 12.d reveal reduced porosity and increased salt crystallisation. Combined with the peak shear strength data in Figure 6.e, it was found that higher water and salt contents enhance shear strength at low temperatures, whereas the opposite trend occurs at elevated temperatures.

From a pore structure perspective, the macroscopic mechanism involves the filling of interconnected and isolated pores within saline soil under low-temperature conditions, thereby increasing the effective stress between particles [24]. At varying water and salt contents, elevated temperatures promote free water accumulation, whereas low temperatures favour bound water retention. The microscopic mechanism involves temperature-induced phase transitions of salts and water within pores: low temperatures drive the propagation of salt and ice crystallisation fronts along interconnected and isolated pores, forming dense cryogenic salt–ice composite structures [25, 26]. Comprehensive analysis indicates that the regulatory mechanism of pore structure evolution on mechanical stability arises from the reconfiguration of three-dimensional pore networks across multiple scales.

3.4.2. Co-evolutionary process of mechanics and microstructure

As shown in Figure 13, the schematic diagram illustrates the co-evolution of the microstructure of saline soil under low-temperature conditions. Driven by multi-physical coupling mechanisms, the microscale structural evolution of the saline soil system can be characterised by four distinct phases. In the initial nucleation stage, supercooling drives heterogeneous nucleation of saline solutions within the mesopores of the soil matrix, where nucleation density is jointly controlled by pore topology constraints and local solution saturation. Upon entering the chain-like growth phase, the thermo-mechanical coupling field induces oriented epitaxial growth of crystal nuclei along the maximum principal stress axis, preferentially aligned towards the cold end of the specimen. The ions formed after salt dissolution (such as Na^+ and Cl^-) disrupt the hydrogen-bond network between water molecules, interfere with the regular arrangement of ice crystals, and depress the freezing point. This process establishes a three-dimensional penetrating dendritic network, whose spatial connectivity triggers a stepwise enhancement of compressive strength [27, 28]. During the dynamic reconstruction stage, free water is converted into bound water through interfacial adsorption, promoting secondary salt crystallisation and reorganisation into a face-centred cubic (FCC) lattice (space group Fm3m) via Ostwald ripening mechanisms, marking the onset of a strength stabilisation regime [29, 30]. The final critical failure stage involves stress concentration-induced fractal propagation of microcracks along maximum shear stress planes, culminating in extensive structural collapse [31–33]. Notably, during temperature reversal, this evolution follows a thermal activation-dominated degradation pathway, in which lattice dissociation releases bound water to reconstruct pore networks, resulting in an exponential correlation between the strength decay rate and temperature.

3.4.3. Relationship between pore coordination number and mechanical strength

As shown in Figure 14, the coordination numbers of specimens with different water and salt contents (w_1–s_1, w_2–s_2, w_3–s_3, w_4–s_4), are presented, where the pore coordination number represents the number of throats connected to pore channels. The figure demonstrates that, as salt and water contents increase, the pore space becomes more abundant in the spatial distribution. Here, discretised spherical units represent pore spaces, while tubular connectors characterise throat structures. Pore network modelling serves as a core method in cross-scale research on porous media, acting as a bridging framework to correlate microscopic pore topology with macroscopic mechanical responses [34–36]. Through node connectivity and coordination numbers, this approach quantitatively reveals the regulatory mechanisms by which pore space connectivity influences mechanical properties, as well as the multi-scale correlations between pore-level structural evolution and macroscopic mechanical responses [37, 38].

The coordination number is a microscopic parameter characterising pore connectivity. Its numerical variation directly regulates the mass transport and mechanical response mechanisms of the pore system. When the coordination number is zero, pores exist in an isolated and closed state. Although they can store water and salts to form localised enrichment zones,

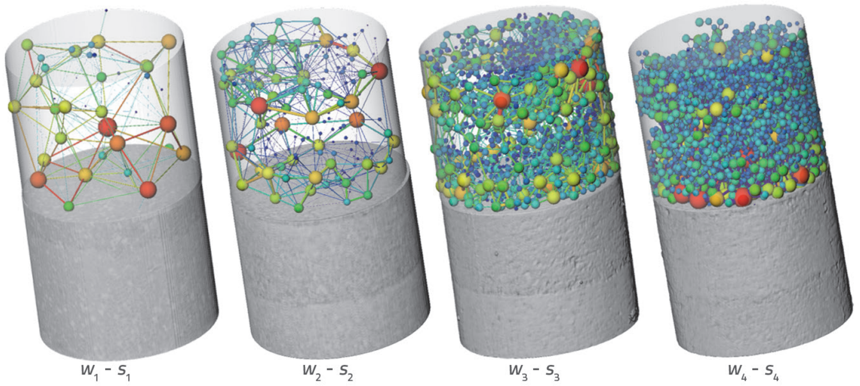

Figure 14. Equivalent pore network model

their contribution to water–salt migration is minimal [39, 40]. A higher coordination number indicates better pore connectivity, more migration pathways for water–salt transport, reduced tortuosity between pores and throats, and enhanced water–salt mobility [41]. Figures 14.a to 14.d show pore coordination number density cloud diagrams. These figures reveal that, as salt and water contents increase, the coordination number density within the 0–25 range increases, indicating that higher water and salt contents improve the connectivity of the pore structure in the specimens. Isolated pores, being disconnected from the external pore network, generate high internal stresses due to ice volume expansion. This stress can cause pore wall rupture or the propagation of existing microcracks, thereby altering pore shapes and sizes [42–45]. Under applied loads, higher coordination numbers correspond to more particle contact points, allowing external forces to dissipate through multiple pathways and reducing localised stress concentrations. Additionally, dense particle contact networks resist shear deformation, inhibiting particle slippage or rotation [46].

4. Multiscale coupled strength model construction

4.1. Quantitative model for dynamic shear modulus attenuation

The dynamic shear modulus is a critical mechanical indicator for railway subgrades; therefore, a degradation quantification model for the dynamic shear modulus was established [47, 48]. Based on soil dynamics theory and multi-factor coupling effects, an expression for the dynamic shear modulus was derived, as shown in Equation (1).

$$G_d = G_0 \cdot f(w) \cdot g(s) \cdot h(t) \cdot k(d) \tag{1}$$

where G_0 represents the reference dynamic shear modulus, $f(w)$ is the moisture content attenuation function, $g(s)$ is the salt content enhancement coefficient, $h(t)$ is the temperature gradient response function, $k(d)$ is the dynamic stress hardening function.

The functional forms and parameters were calibrated using experimental data. Specifically, the water content attenuation function was derived to analyse the influence of water content (w) on the dynamic shear modulus (G_d) [49, 50]. For a fixed set of experimental conditions (salt content s = 0 %, temperature = 40 °C, dynamic stress amplitude = 50 kPa), the dynamic shear modulus values were determined as follows: G_d = 29 MPa at w = 4 %, G_d = 27 MPa at w = 6 %, G_d = 25 MPa at w = 8 %, and G_d = 21 MPa at w = 10 %.

An exponential decay model, Equation (2) was adopted for curve fitting. The data were linearised by logarithmic transformation

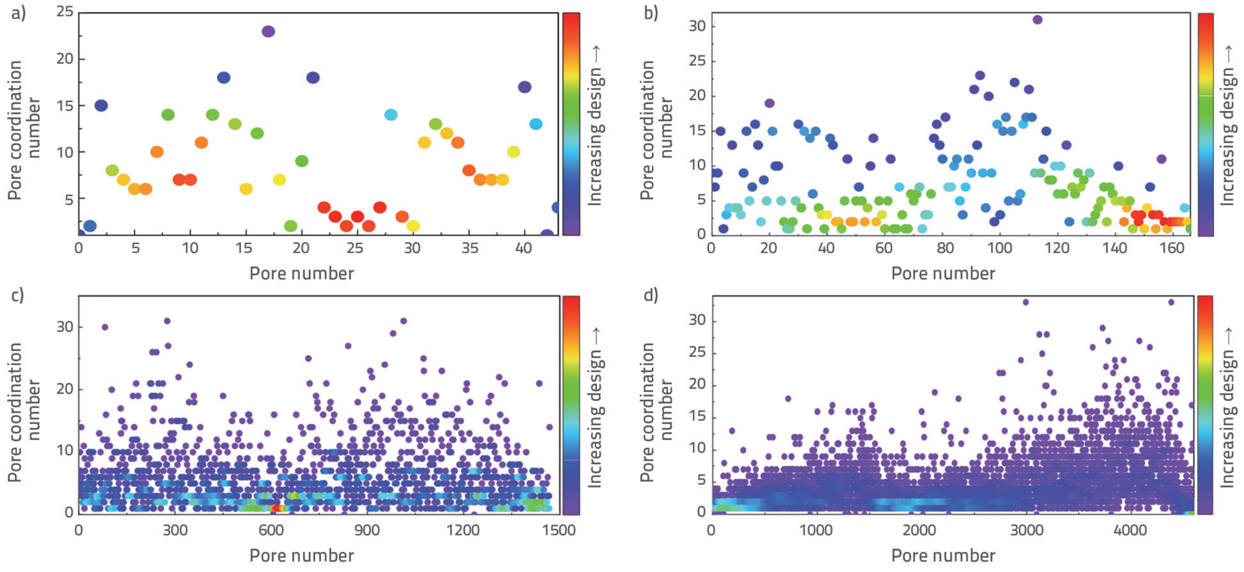

Figure 15. Pore coordination number density contour maps: a) w_1–s_1; b) w_2–s_2; c) w_3–s_3; d) w_4–s_4

(Equation 3), with w_o = 4 % defined as the reference water content. Parameter calibration using the least-squares method yielded β = 0.042 $\%^{-1}$, indicating a modulus attenuation rate of approximately 4.2 % per 1 % increase in water content.

$$f(w) = e - b(w-w_0) \tag{2}$$

$$\ln\left(\frac{G_d}{G_0}\right) = -\beta(w-0{,}04) \tag{3}$$

The salt content enhancement function $g(s)$ was established to analyse the influence of salt content (s) on the dynamic shear modulus. Under fixed experimental conditions (water content w = 4 %, temperature T = –20 °C, dynamic stress amplitude = 200 kPa), the dynamic shear modulus corresponding to s = 0 % was normalised as the reference value [51]. Normalisation refers to the process of adjusting data with different dimensions or scales to a unified interval through mathematical transformation. A linear enhancement model (Equation (5)) was derived based on Equation (4). Substituting the experimental data into Equation (5) yielded 831 = 29 · (1+α · 0.15), from which α = 0.1135^{-1} is obtained. This indicates that each 1 % increase in salt content enhances the modulus by approximately 11.3 %.

$$G_d = 831 \cdot \frac{29}{831} = 29\,(\text{Normalization}) \tag{4}$$

$$g(s) = 1 + \alpha s \tag{5}$$

Establish the temperature gradient response function $h(t)$ with fixed parameters: water content w = 4 %, salt content s = 15 %, and a dynamic stress amplitude of 200 kPa. Let the temperature t = 40 °C be the initial temperature, and the temperature difference be Δt. The dynamic shear modulus was normalised as shown in Equation (6), resulting in the linear temperature-sensitive model given by Equation (7). By combining this with the dynamic term 4^n and solving the equations simultaneously, γ = 0.018 $°C^{-1}$ was obtained. This indicates that for every 1 °C decrease in temperature, the modulus increased by 1.8 %.

$$G_d = 29 \cdot 4^n\,(\text{Normalization}) \tag{6}$$

$$h(t) = 1 + \gamma\Delta \cdot t \tag{7}$$

The dynamic stress hardening function K (D) was established with fixed parameters: water content w = 4 %, salt content s = 15 %, and temperature t = –20 °C. When the dynamic stress amplitude was 50 kPa, the dynamic shear modulus was expressed by Equation (6). Using the power-law model shown in Equation (8), Equation (6) yielded 831 = 29 × 4n. Solving for n gave n = 1.51. Consequently, each doubling of the dynamic stress amplitude increased the modulus by approximately 2.85 times.

$$K(D) = \left(\frac{d}{D_0}\right)^n \tag{8}$$

The complete model expression (Equation (9)) was developed and validated using experimental data. Level 7 was selected with the following parameters: water content w = 6 %, salt content s = 10 %, and temperature t = –20 °C. Substituting these values into Equation (9) yielded Equation (10). The calculated results aligned with the experimental data, confirming the validity of the model.

$$G_d = 29 \cdot e^{-0{,}042(w-4)} \cdot (1+0{,}113s) \cdot (1+0{,}018\Delta t) \cdot (d/50)^{1{,}51} \tag{9}$$

$$G_d = 29 \cdot e^{-0{,}042(6-4)} \cdot (1+0{,}113 \cdot 10) \cdot (1+0{,}018 \cdot 60) \cdot (200/50)^{1{,}51} \approx 206\ \text{MPa} \tag{10}$$

In the equation, w represents the water content (%), with a reference value w_0 = 4 %; s denotes the salt content; Δt is the temperature gradient, defined as Δt = 40 – t, d stands for the dynamic stress amplitude.

5. Conclusion

This study systematically investigated the coupled effects of water, salt, temperature, and mechanical loading on the strength behaviour and microstructural evolution of saline soils through laboratory experiments and multiscale modelling. Based on the experimental results and theoretical analysis, the following conclusions were drawn:

- Under coupled water–salt–thermal–mechanical effects, increases in moisture and salt contents together with decreasing temperature led to increases in mechanical indicators, including shear strength, backbone curve slope, and dynamic shear modulus. Conversely, cumulative plastic strain and damping ratio gradually decreased. The sensitivity ranking of influencing factors showed: moisture content > salt content = temperature for shear strength, backbone curve slope, and dynamic shear modulus; and moisture content > salt content = temperature = dynamic stress amplitude for cumulative plastic strain and damping ratio.
- The low-temperature-induced microstructural evolution of saline soil systems was characterised as a four-stage cascade phase transition process: initial nucleation stage, chain-growth stage, dynamic reconstruction stage, and critical failure stage. With increasing moisture content and temperature, bound water content gradually decreased while free water content increased, with minimal variation observed in capillary water content.
- The synergistic evolution of water–salt–thermal–mechanical multi-field coupled mechanical responses and microstructure was primarily manifested in pore structure evolution and water–salt phase transitions. Saline soils with varying water and salt contents exhibited different pore coordination numbers. At low temperatures, pores with low coordination numbers generated higher internal stresses, whereas pores with high coordination numbers dispersed and transferred stresses through multiple pathways, thereby reducing local stress concentrations. Consequently, the regulatory mechanism of pore structure evolution on mechanical

stability lies in the three-dimensional reconstruction of pore structures under multi-scale environmental conditions.

- A multiscale coupled strength model for saline soil was established through the systematic accumulation of experimental data and the integration of cross-scale theories to develop a degradation quantification model. Laboratory orthogonal experiments revealed mechanical response characteristics under four-field coupling conditions (water, salt, heat, and stress), providing critical parameter boundary conditions for constructing the coupling equations.

  The established attenuation model enables the prediction of railway subgrade mechanical responses under four-field interactions, providing a theoretical reference for preventing saline soil hazards in railway engineering.

Acknowledgements

The project is supported by the National Natural Science Foundation of China Railway Basic Research Joint Fund (U2568210).

REFERENCES

[1] Li, C.J., Liu, R., et al.: Growth and sustainability of suaeda salsa in the Lop Nur, China, Journal of Arid Land, 10 (2018) 3, pp. 429-440, https://doi.org/10.10.1007/s40333-018-0002-5

[2] Zhang, S.S., Zhang, J.S., et al.: Deformation properties of coarse-grained sulfa the saline soil under the freeze thaw-precipitation cycle, Cold Regions Science and Technology, 177 (2020), pp. 103-121, https://doi.org/10.1016/j.coldregions.2020.103121

[3] Liao, X., Fan, M.J., et al.: Cumulative deformation characteristics of saline-alkali soil in Lop Nur under freeze-thaw cycling, Geology Journal of Engineering, 32 (2024) 3, pp. 800-810, https://dx.doi.org/10.13544/j.cnki.jeg.2023-0255

[4] Zhang, J., Lai, Y.M., et al.: Study on the influence of hydro-thermal-salt-mechanical interaction in saturated frozen sulfate saline soil based on crystallization kinetics, International Journal of Heat and Mass Transfer, 146 (2020), pp. 1188-68, https://doi.org/10.1016/j.ijheatmasstransfer.2019.118868

[5] Chen, H., Gao, X., Wang, Q.: Research progress and prospect of frozen soil engineering disasters, Cold Regions Science and Technology, 212 (2023), pp. 103901, https://doi.org/10.1016/j.coldregions.2023.103901

[6] Xu, J., Lan, W., Ren, C., et al.: Modeling of coupled transfer of water, heat and solute in saline loess considering sodium sulfate crystallization, Cold Regions Science and Technology, 189 (2021), pp. 1033-35, https://doi.org/10.1016/j.coldregions.2021.103335

[7] Zhang, X.D., Zhai, E.C., et al.: Theoretical and numerical analyses on hydro-thermal-salt-mechanical interaction of unsaturated salinized soil subjected to typical unidirectional freezing process, International Journal of Geomechanics, 21 (2021) 7, pp. 20-36, https://doi.org/10.1061/ (ASCE) GM.1943-5622.0002036

[8] Vranešić, K., Haladin, I., Burnać, K.: Influence of climate changes on railway superstructure. GRAĐEVINAR, 77 (2025) 1, pp. 43-67, https://doi.org/10.14256/JCE.4123.2024

[9] Jovanović, S., Guler, H., Čoko, B.: Track degradation analysis in the scope of railway infrastructure maintenance management systems, GRAĐEVINAR, 67 (2015) 3, pp. 247-258, https://doi.org/10.14256/JCE.1194.2014

[10] Chen, Y.Y., Lai, Y.M., et al.: Finite element analysis of heat and mass transfer in unsaturated freezing soils: formulation and verification, Computers and Geotechnics, 149 (2022), pp. 1048-48, https://doi.org/10.1016/j.compgeo.2022.104848

[11] Chen, M., Liu, R.S., Dong, Z.: Effect of different chloride salts on the transport of water, heat, and solutes in sandy soil under freezing conditions, Journal of Cold Regions Engineering, 37 (2023) 3, pp. 040230-13, https://doi.org/10.1061/JCRGEI.CRENG-650

[12] Zhang, T., Yang, Y.L.: A shear model for solidified soils considering conservation of energy, Computers and Geotechnics, 120 (2020) :103439, https://doi.org/10.1016/j.compgeo.2020.103439

[13] Zhou, F.X., Gao, G.Y.: Steady-state analysis of the heat-moisture-salt coupling for unsaturated soil. Rock and Soil Mechanics, 40 (2019) 6, pp. 2050-2058. (in Chinese).

[14] Luo, C.L., Yu, Y.Y., et al.: Thermal-water-salt coupling process of unsaturated saline soil under unidirectional freezing, Journal of Mountain Science, 20 (2023) 2, pp. 557-569, https://doi.org/10.1007/s11629-022-7652-7

[15] Li, S., Chen, H., Chen, Z.: Water and salt migration characterization in NaHCO$_3$ saline soils during unidirectional freezing conditions, Cold Regions Science and Technology, 213 (2023), pp. 103940, https://doi.org/10.1016/j.coldregions.2023.103940

[16] Zhang, J., Lai, Y.M., et al.: Numerical study on the hydro-thermal-chemical-mechanical coupling mechanism in sulfate saline soil under freeze-thaw cycles, Computers and Geotechnics, 176 (2024), pp. 106803, https://doi.org/10.1016/j.compgeo.2024.106803

[17] Zhang, Q.S., Dong, J.L., et al.: Dynamic stress response in a novel prestressed subgrade under heavy-haul train loading: A numerical analysis, Construction and Building Materials, 412 (2024), pp. 134749, https://doi.org/10.1016/j.conbuildmat.2023.134749

[18] Zhang, T., Liu, S., Zhan, H., et al. 2020. Durability of silty soil stabilized with recycled lignin for sustainable engineering materials, Journal of Cleaner Production, 248 (2020), pp. 119293. https://doi.org/10.1016/j.jclepro.2019.119293

[19] Setia, R., Rengasamy, P., Marschner, P.: Effect of exchangeable cation concentration on sorption and desorption of dissolved organic carbon in saline soil, Science of The Total Environment, 465 (2013), pp. 226-232, https://doi.org/10.1016/j.scitotenv.2013.01.010

[20] Han, Y., Wang, Q., et al.: Effect of freeze-thaw cycles on shear strength of saline soil, Cold Regions Science and Technology, 154 (2018), pp. 42-53, https://doi.org/10.1016/j.coldregions.2018.06.002

[21] Chen, Q., Peng, Y.L., et al.: Experimental study on dynamic characteristics of expansive soil from Yanzhou-Shijiusuo railway roadbed under eyelid loading, Journal of Engineering Geology, 27 (2019) 4, pp. 737-744(in Chinese).

[22] Liu, W.Z., Wan, J.L., et al.: Accumulative deformation characteristics of lateritic clay under combined action of cyclic wetting and dynamic loading, China Journal of Highway and Transport, 35 (2022) 8, pp. 129-139, https://doi.org/10.13544/j.cnki.xq2019030

[23] Shen, J.J., Wang, Q., et al.: Experimental investigation into the salinity effect on the physicomechanical properties of carbonate saline soil, Journal of Rock Mechanics and Geotechnical Engineering, 16 (2024) 5, pp. 1883-1895, https://doi.org/10.1016/j.jrmge.2023.09.024

[24] Liu, W.Z., Xu, Y., et al.: Experimental study on dynamic response and accumulated deformation of improved expansive soil under wetting action in heavy-oaded railway, Journal of Railway Engineering Society. 45 (2013) 2, pp. 127-138,(in Chinese).

[25] You, Z.M., Wen, W., et al.: Model tests of the barrier measures on moisture and salt migration in soils subjected to freeze-thaw cycle, Cold Regions Science and Technology, 201 (2022), pp. 103607, https://doi.org/10.1016/j.coldregions.2022.103607

[26] Shen, J., Wang, Q., Chen, Y., et al.: Evolution process of the microstructure of saline soil with different compaction degrees during freeze-thaw cycles, Engineering Geology, 304 (2022), pp. 106699, https://doi.org/10.1016/j.enggeo.2022.106699

[27] Xiao, Z.A., Li, K.L., et al.: Study on the multi-field-coupling model of saline frozen soil considering ice and salt crystallization, Computers and Geotechnics, 169 (2024), pp. 106209, https://doi.org/10.1016/j.compgeo.2024.106209

[28] Han, M.X., Peng, W., et al.: Micro-composition evolution of the undisturbed saline soil undergoing different freeze-thaw cycles, Cold Regions Science and Technology, 210 (2023), pp.103825, https://doi.org/10.1016/j.coldregions.2023.103825

[29] Wang, C., Lai, Y.M., et al.: Estimating the freezing-thawing hysteresis of chloride saline soils based on the phase transition theory B Applied Thermal Engineering, 135 (2018), pp. 22-33, https://doi.org/10.1016/j.applthermaleng.2018.02.039

[30] Xiong, Q.X., Tong, L.Y., et al.: Salt crystallization in porous materials: A quasi-local transport model for evaluating pore filling process, Construction and Building Material, 462 (2025), pp. 139904, https://doi.org/10.1016/j.conbuildmat.2025.139904

[31] Michael, S., Sönke, A.: Crystallization of sodium sulfate phases in porous materials: The phase diagram Na_2SO_4-H_2O and the generation of stress, Geochimicaet Cosmochimica Acta, 72 (2008) 17, pp. 4291-4306, https://doi.org/10.1016/j.gca.2008.05.053

[32] Elzbieta, P., Albert, V.: Studying ice with environmental scanning electron microscopy, Molecules, 27 (2022), pp. 10258, https://doi: 10.3390/molecules27010258

[33] Tong, F.G., Jing, L.R., et al.: A fully coupled thermo-hydro-mechanical model for simulating multiphase flow, deformation and heat transfer in buffer material and rock masses, International Journal of Rock Mechanics and Mining Sciences, 47 (2010) 2, pp. 205-217, https://doi.org/10.1016/j.ijrmms.2009.11.002.

[34] Munkholm, L., Heck, R., Deen, B.: Soil pore characteristics assessed from X-ray micro-CT derivedimages and correlations to soil friability, Geoderma, 181 (2012), pp. 22-29, https://doi.org/10.1016/j.geoderma.2012.02.024

[35] Peitgen, H.O., Jürgens, H., Saupe, D.: Chaos and fractals: New frontiers of science (1992) New York: Springer.

[36] Mali, P.: Multifractal characterization of global temperature anomalies, Theoretical and Applied Climatology, 121 (2015) 3, pp. 641-648, https://doi.org/10.1007/s00704-014-1268-y

[37] Sun, X.Q., She, D.L., et al.: Three-dimensional fractal characteristics of soil pore structure and their relationships with hydraulic parameters in biochar-amended saline soil, Soil and Tillage esearch, 205 (2020), pp. e104809, https://doi.org/10.1016/j.still.2020.104809

[38] Soto-Gomez, D., Perez-Rodriguez, P., et al.: 3D multifractal characterization of computed tomography images of soils under different tillage management: Linking multifractal parameters to physical propertie, Geoderma, 363 (2020), pp. e114129, https://doi.org/10.1016/j.geoderma.2019.114129

[39] Masanobu, O.: Coordination number and its relation to shear strength of granular material, Soils and Foundation, 17 (1997) 2, pp. 29-42, https://doi.org/10.3208/sandf1972.17.2_29.

[40] Korvin, G.: Coordination Number of Grains. In: Statistical Rock Physics, Earth and Environmental Sciences Library. Springer, Cham. https://doi.org/10.1007/978-3-031-46700-4_6.

[41] McDowell, G., Lim, W.: The importance of coordination number in using agglomerates to simulate crushable particles in the discrete element method, Géotechnique, 57 (2007) 8, pp.701-705, https://doi.org/10.1680/geot.2007.57.8.701.

[42] Salami, Y., Dano, C., Hicher, P.Y.: An experimental study on the influence of the coordination number on grain crushing, European Journal of Environmental and Civil Engineering, 23 (2017) 3, pp. 432-448, https://doi.org/10.1080/19648189.2017.1285251

[43] Wan, X.S., Zhou, H., et al.: Mesoscopic shear evolution characteristics of frozen soil-concrete interface, Cold Regions Science and Technology, 229 (2025), pp. 104342, https://doi.org/10.1016/j.coldregions.2024.104342

[44] Zi, J.J., Liu, T., Zhang, W., et al.: Quantitatively characterizing sandy soil structure altered by MICP using multi-level thresholding segmentation algorithm, Journal of Rock Mechanics and Geotechnical Engineering. 16 (2023) 10, pp. 4285-4299, https://doi.org/10.1016/j.jrmge.2023.11.025

[45] Wright, V., Ferrick, A., Manga, M., et al.: Coordination numbers in natural beach sand, EPJ Web of Conferences, 249 (2021), pp. 11008, https://doi.org/10.1051/epjconf/202124911008

[46] Wang, G., Wei, J.T.: Microstructure evolution of granular soils in cyclic mobility and post-liquefaction process, Granular Matter, 18 (2016) 51, pp. 621-625, https://doi.org/10.1007/s10035-016-0621-5

[47] Wichtmann, T., Niemunis, A., et al.: Strain accumulation in sand due to cyclic loading: drained triaxial tests, Soil Dynamics and Earthquake Engineering, 25 (2005) 12, pp. 967-979, https://doi.org/10.1016/j.soildyn.2005.02.022

[48] Yaser, J., Hamed J., Abdolhosein, H.: Dynamic properties of calcareous and siliceous sands under isotropic and anisotropic stress conditions, Soils and Foundations, 58 (2018), pp. 172-184, https://doi.org/10.1016/j.sandf.2017.11.010

[49] Ran, H., Liu, H.H., et al.: A constitutive model for unsaturated soils with consideration of inter-particle bonding, Computers and Geotechnics, 59 (2014), pp. 127-144. https://doi.org/10.1016/j.compgeo.2014.03.007

[50] Wang, X., Xia, T., et al.: Effect of soil microstructure on the small-strain shear modulus of saline soil, Arabian Journal of Geosciences, 14 (2021) 1, pp. 06304, https://doi.org/10.1007/s12517-020-06304-8

[51] Yu, Y.Y., Luo, C.L., Cui, W.H., et al.: Study on creep characteristics and component model of saline soil in hexi corridor, Scientific Reports, 13 (2023), pp. 18067, https://doi.org/10.1038/s41598-023-42548-6